Eur. Phys. J. C 28, 437–449 (2003)
Digital Object Identifier (DOI) 10.1140/epjc/s2003-01201-x

THE EUROPEAN PHYSICAL JOURNAL C

Measurement of the inclusive $D^{*\pm}$ production in $\gamma\gamma$ collisions at LEP

The ALEPH Collaboration

A. Heister, S. Schael
Physikalisches Institut das RWTH-Aachen, 52056 Aachen, Germany

R. Barate, R. Brunelière, I. De Bonis, D. Decamp, C. Goy, S. Jezequel, J.-P. Lees, F. Martin, E. Merle, M.-N. Minard, B. Pietrzyk, B. Trocmé
Laboratoire de Physique des Particules (LAPP), IN^2P^3-CNRS, 74019 Annecy-le-Vieux Cedex, France

S. Bravo, M.P. Casado, M. Chmeissani, J.M. Crespo, E. Fernandez, M. Fernandez-Bosman, Ll. Garrido[15], M. Martinez, A. Pacheco, H. Ruiz
Institut de Física d'Altes Energies, Universitat Autònoma de Barcelona, 08193 Bellaterra (Barcelona), Spain[7]

A. Colaleo, D. Creanza, N. DeFilippis, M. dePalma, G. Iaselli, G. Maggi, M. Maggi, S. Nuzzo, A. Ranieri, G. Raso[24], F. Ruggieri, G. Selvaggi, L. Silvestris, P. Tempesta, A. Tricomi[3], G. Zito
Dipartimento di Fisica, INFN Sezione di Bari, 70126 Bari, Italy

X. Huang, J. Lin, Q. Ouyang, T. Wang, Y. Xie, R. Xu, S. Xue, J. Zhang, L. Zhang, W. Zhao
Institute of High Energy Physics, Academia Sinica, Beijing, P.R. China[8]

D. Abbaneo, P. Azzurri, T. Barklow[26], O. Buchmüller[26], M. Cattaneo, F. Cerutti, B. Clerbaux[23], H. Drevermann, R.W. Forty, M. Frank, F. Gianotti, J.B. Hansen, J. Harvey, D.E. Hutchcroft, P. Janot, B. Jost, M. Kado[2], P. Mato, A. Moutoussi, F. Ranjard, L. Rolandi, D. Schlatter, G. Sguazzoni, W. Tejessy, F. Teubert, A. Valassi, I. Videau, J.J. Ward
European Laboratory for Particle Physics (CERN), 1211 Geneva 23, Switzerland

F. Badaud, S. Dessagne, A. Falvard[20], D. Fayolle, P. Gay, J. Jousset, B. Michel, S. Monteil, D. Pallin, J.M. Pascolo, P. Perret
Laboratoire de Physique Corpusculaire, Université Blaise Pascal, IN^2P^3-CNRS, Clermont-Ferrand, 63177 Aubière, France

J.D. Hansen, J.R. Hansen, P.H. Hansen, A. Kraan, B.S. Nilsson
Niels Bohr Institute, 2100 Copenhagen, Denmark[9]

A. Kyriakis, C. Markou, E. Simopoulou, A. Vayaki, K. Zachariadou
Nuclear Research Center Demokritos (NRCD), 15310 Attiki, Greece

A. Blondel[12], J.-C. Brient, F. Machefert, A. Rougé, M. Swynghedauw, R. Tanaka H. Videau
Laoratoire Leprince-Ringuet, Ecole Polytechnique, IN^2P^3-CNRS, 91128 Palaiseau Cedex, France

V. Ciulli, E. Focardi, G. Parrini
Dipartimento di Fisica, Università di Firenze, INFN Sezione di Firenze, 50125 Firenze, Italy

A. Antonelli, M. Antonelli, G. Bencivenni, F. Bossi, G. Capon, V. Chiarella, P. Laurelli, G. Mannocchi[5], G.P. Murtas, L. Passalacqua
Laboratori Nazionali dell'INFN (LNF-INFN), 00044 Frascati, Italy

J. Kennedy, J.G. Lynch, P. Negus, V. O'Shea, A.S. Thompson
Department of Physics and Astronomy, University of Glasgow, Glasgow G12 8QQ, UK[10]

S. Wasserbaech
Department of Physics, Haverford College, Haverford, PA 19041-1392, USA

R. Cavanaugh[4], S. Dhamotharan[21], C. Geweniger, P. Hanke, V. Hepp, E.E. Kluge, G. Leibenguth, A. Putzer, H. Stenzel, K. Tittel, M. Wunsch[19]
Kirchhoff-Institut für Physik, Universität Heidelberg, 69120 Heidelberg, Germany[16]

R. Beuselinck, W. Cameron, G. Davies, P.J. Dornan, M. Girone[1], R.D. Hill, N. Marinelli, J. Nowell, S.A. Rutherford, J.K. Sedgbeer, J.C. Thompson[14], R. White
Department of Physics, Imperial College, London SW7 2BZ, UK[10]

V.M. Ghete, P. Girtler, E. Kneringer, D. Kuhn, G. Rudolph
Institut für Experimentalphysik, Universität Innsbruck, 6020 Innsbruck, Austria[18]

E. Bouhova-Thacker, C.K. Bowdery, D.P. Clarke, G. Ellis, A.J. Finch, F. Foster, G. Hughes, R.W.L. Jones, M.R. Pearson, N.A. Robertson, M. Smizanska
Department of Physics, University of Lancaster, Lancaster LA1 4YB, UK[10]

O. van der Aa, C. Delaere[28], V. Lemaitre[29]
Institut de Physique Nucléaire, Département de Physique, Université Catholique de Louvain, 1348 Louvain-la-Neuve, Belgium

U. Blumenschein, F. Hölldorfer, K. Jakobs, F. Kayser, K. Kleinknecht, A.-S. Müller, B. Renk, H.-G. Sander, S. Schmeling, H. Wachsmuth, C. Zeitnitz, T. Ziegler
Institut für Physik, Universität Mainz, 55099 Mainz, Germany[16]

A. Bonissent, P. Coyle, C. Curtil, A. Ealet, D. Fouchez, P. Payre, A. Tilquin
Centre de Physique des Particules de Marseille, Univ Méditerranée, IN^2P^3-CNRS, 13288 Marseille, France

F. Ragusa
Dipartimento di Fisica, Università di Milano e INFN Sezione di Milano, 20133 Milano, Italy

A. David, H. Dietl, G. Ganis[27], K. Hüttmann, G. Lütjens, W. Männer, H.-G. Moser, R. Settles, G. Wolf
Max-Planck-Institut für Physik, Werner-Heisenberg-Institut, 80805 München, Germany[16]

J. Boucrot, O. Callot, M. Davier, L. Duflot, J.-F. Grivaz, Ph. Heusse, A. Jacholkowska[6], L. Serin, J.-J. Veillet, C. Yuan
Laboratoire de l'Accélérateur Linéaire, Université de Paris-Sud, IN^2P^3-CNRS, 91898 Orsay Cedex, France

G. Bagliesi, T. Boccali, L. Foà, A. Giammanco, A. Giassi, F. Ligabue, A. Messineo, F. Palla, G. Sanguinetti, A. Sciabà, R. Tenchini[1], A. Venturi[1], P.G. Verdini
Dipartimento di Fisica dell'Università, INFN Sezione di Pisa, e Scuola Normale Superiore, 56010 Pisa, Italy

O. Awunor, G.A. Blair, G. Cowan, A. Garcia-Bellido, M.G. Green, L.T. Jones, T. Medcalf, A. Misiejuk, J.A. Strong, P. Teixeira-Dias
Department of Physics, Royal Holloway & Bedford New College, University of London, Egham, Surrey TW20 OEX, UK[10]

R.W. Clifft, T.R. Edgecock, P.R. Norton, I.R. Tomalin
Particle Physics Dept., Rutherford Appleton Laboratory, Chilton, Didcot, Oxon OX11 OQX, UK[10]

B. Bloch-Devaux, D. Boumediene, P. Colas, B. Fabbro, E. Lançon, M.-C. Lemaire, E. Locci, P. Perez, J. Rander, B. Tuchming, B. Vallage
CEA, DAPNIA/Service de Physique des Particules, CE-Saclay, 91191 Gif-sur-Yvette Cedex, France[17]

N. Konstantinidis, A.M. Litke, G. Taylor
Institute for Particle Physics, University of California at Santa Cruz, Santa Cruz, CA 95064, USA[22]

C.N. Booth, S. Cartwright, F. Combley[25], P.N. Hodgson, M. Lehto, L.F. Thompson
Department of Physics, University of Sheffield, Sheffield S3 7RH, UK[10]

A. Böhrer, S. Brandt, C. Grupen, J. Hess, A. Ngac, G. Prange, U. Sieler[30]
Fachbereich Physik, Universität Siegen, 57068 Siegen, Germany[16]

C. Borean, G. Giannini
Dipartimento di Fisica, Università di Trieste e INFN Sezione di Trieste, 34127 Trieste, Italy

H. He, J. Putz, J. Rothberg
Experimental Elementary Particle Physics, University of Washington, Seattle, WA 98195, USA

S.R. Armstrong, K. Berkelman, K. Cranmer, D.P.S. Ferguson, Y. Gao[13], S. González, O.J. Hayes, H. Hu, S. Jin, J. Kile, P.A. McNamara III, J. Nielsen, Y.B. Pan, J.H. von Wimmersperg-Toeller, W. Wiedenmann, J. Wu, Sau Lan Wu, X. Wu, G. Zobernig
Department of Physics, University of Wisconsin, Madison, WI 53706, USA[11]

G. Dissertori
Institute for Particle Physics, ETH Hönggerberg, 8093 Zürich, Switzerland

Received: 13 January 2003 /
Published online: 13 May 2003 –

Abstract. The inclusive production of $D^{*\pm}$ mesons in two-photon collisions is measured with the ALEPH detector at e^+e^- centre-of-mass energies from 183 GeV to 209 GeV. A total of 360 ± 27 $D^{*\pm}$ meson events are observed from an integrated luminosity of 699 pb^{-1}. Contributions from direct and single-resolved processes are separated using the ratio of the transverse momentum $p_t^{D^{*\pm}}$ of the $D^{*\pm}$ to the visible invariant mass W_{vis} of the event. Differential cross sections of $D^{*\pm}$ production as functions of $p_t^{D^{*\pm}}$ and the pseudorapidity $|\eta^{D^{*\pm}}|$ are measured in the range $2\,\mathrm{GeV}/c < p_t^{D^{*\pm}} < 12\,\mathrm{GeV}/c$ and $|\eta^{D^{*\pm}}| < 1.5$. They are compared to next-to-leading order (NLO) perturbative QCD calculations. The extrapolation of the integrated visible $D^{*\pm}$ cross section to the total charm cross section, based on the Pythia Monte Carlo program, yields $\sigma(e^+e^- \to e^+e^- c\bar{c})_{\langle\sqrt{s}\rangle=197\,\mathrm{GeV}} = 731 \pm 74_{stat} \pm 47_{syst} \pm 157_{extr}$ pb.

1 Introduction

Heavy flavour production in two-photon events at LEP 2 centre-of-mass energies is dominated by charm production processes in which both of the photons couple directly to the charm quark (*direct processes*) or in which one photon couples directly and the other appears resolved (*single-resolved processes*) (Fig. 1) [1]. These two contributions are of the same order of magnitude within the experimental acceptance. Because the single-resolved process is dominated by γg fusion, the measurement of the cross section can give access to the gluon content of the photon. Moreover, the large masses of the c and b quarks provide a cutoff for perturbative QCD calculations, allowing a good test of QCD predictions for the corresponding reactions. Contributions from processes in which both photons appear resolved (*double-resolved processes*) are suppressed by more than two orders of magnitude compared to the total cross section [1]. The production of b quark is expected to be suppressed by a large factor compared to charm quark because of the heavier mass and smaller absolute charge.

In the present analysis charm production is measured in two steps. A high-purity $\gamma\gamma$ sample is first selected, then examined for its charm content via reconstruction of D^{*+} mesons in their decay to $D^0\pi^+$. This letter is organized as follows. A short description of the ALEPH detector is given in Sect. 2. Monte Carlo simulations for signal and background processes are described in Sect. 3. In Sect. 4,

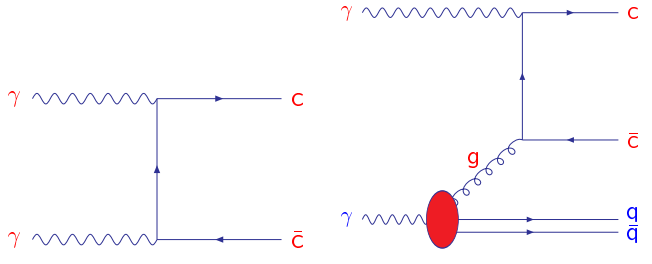

a Direct process **b** Single-resolved process

Fig. 1a,b. Main contributions to charm production in $\gamma\gamma$ events

[1] Also at CERN, 1211 Geneva 23, Switzerland
[2] Now at Fermilab, PO Box 500, MS 352, Batavia, IL 60510, USA
[3] Also at Dipartimento di Fisica di Catania and INFN Sezione di Catania, 95129 Catania, Italy
[4] Now at University of Florida, Department of Physics, Gainesville, Florida 32611-8440, USA
[5] Also Istituto di Cosmo-Geofisica del C.N.R., Torino, Italy
[6] Also at Groupe d'Astroparticules de Montpellier, Université de Montpellier II, 34095, Montpellier, France
[7] Supported by CICYT, Spain
[8] Supported by the National Science Foundation of China
[9] Supported by the Danish Natural Science Research Council
[10] Supported by the UK Particle Physics and Astronomy Research Council
[11] Supported by the US Department of Energy, grant DE-FG0295-ER40896
[12] Now at Departement de Physique Corpusculaire, Université de Genève, 1211 Genève 4, Switzerland
[13] Also at Department of Physics, Tsinghua University, Beijing, The People's Republic of China
[14] Supported by the Leverhulme Trust
[15] Permanent address: Universitat de Barcelona, 08208 Barcelona, Spain
[16] Supported by Bundesministerium für Bildung und Forschung, Germany
[17] Supported by the Direction des Sciences de la Matière, C.E.A
[18] Supported by the Austrian Ministry for Science and Transport
[19] Now at SAP AG, 69185 Walldorf, Germany
[20] Now at Groupe d' Astroparticules de Montpellier, Université de Montpellier II, 34095 Montpellier, France
[21] Now at BNP Paribas, 60325 Frankfurt am Mainz, Germany
[22] Supported by the US Department of Energy, grant DE-FG03-92ER40689
[23] Now at Institut Inter-universitaire des hautes Energies (IIHE), CP 230, Université Libre de Bruxelles, 1050 Bruxelles, Belgique
[24] Also at Dipartimento di Fisica e Tecnologie Relative, Università di Palermo, Palermo, Italy
[25] Deceased
[26] Now at SLAC, Stanford, CA 94309, USA
[27] Now at INFN Sezione di Roma II, Dipartimento di Fisica, Università di Roma Tor Vergata, 00133 Roma, Italy
[28] Research Fellow of the Belgium FNRS
[29] Research Associate of the Belgium FNRS
[30] Now at Verdi Information Consult GmbH, 53757 Sankt Augustin, Germany

event selection and reconstruction of D^{*+} mesons are discussed. The results of the analysis are presented in Sect. 5. Finally, in Sect. 6 a summary is given. Throughout this letter charge-conjugated particles and their decays are implicitly included.

2 ALEPH detector

The ALEPH detector has been described in detail in [2, 3]. Here, only the parts essential to the present analysis are covered briefly. The central part of the ALEPH detector is dedicated to the reconstruction of the trajectories of charged particles. The trajectory of a charged particle emerging from the interaction point is measured by a two-layer silicon strip vertex detector (VDET), a cylindrical drift chamber (ITC) and a large time projection chamber (TPC). The three tracking detectors are immersed in a 1.5 T axial magnetic field provided by a superconducting solenoidal coil. Together they measure charged particle transverse momenta with a resolution of $\delta p_{\mathrm{t}}/p_{\mathrm{t}} = 6\times10^{-4} p_{\mathrm{t}} \oplus 0.005$ (p_{t} in GeV/c). The TPC also provides a measurement of the specific ionization $\mathrm{d}E/\mathrm{d}x_{\mathrm{meas}}$. An estimator $\chi_{\mathrm{h}} = (\mathrm{d}E/\mathrm{d}x_{\mathrm{meas}} - \mathrm{d}E/\mathrm{d}x_{\mathrm{exp,h}})/\sigma_{\mathrm{exp,h}}$ is formed to test a particle hypothesis, where $\mathrm{d}E/\mathrm{d}x_{\mathrm{exp,h}}$ and $\sigma_{\mathrm{exp,h}}$ denote the expected specific ionization and the estimated uncertainty for the particle hypothesis h, respectively. A mass hypothesis may be tested by means of the χ_{h} values themselves or by calculating χ^2_{h} confidence levels P_{h}.

Photons are identified in the electromagnetic calorimeter (ECAL), situated between the TPC and the coil. The ECAL is a lead/proportional-tube sampling calorimeter segmented in $0.9^\circ \times 0.9^\circ$ projective towers and read out in three sections in depth. It has a total thickness of 22 radiation lengths and yields a relative energy resolution of $0.18/\sqrt{E} + 0.009$, with E in GeV, for isolated photons. Electrons are identified by their transverse and longitudinal shower profiles in ECAL and their specific ionization in the TPC.

The iron return yoke is instrumented with 23 layers of streamer tubes and forms the hadron calorimeter (HCAL). The latter provides a relative energy resolution of charged and neutral hadrons of $0.85/\sqrt{E}$, with E in GeV. Muons are distinguished from hadrons by their characteristic pattern in HCAL and by the muon chambers, composed of two double-layers of streamer tubes outside HCAL.

Two small-angle calorimeters, the luminosity calorimeter (LCAL) and the silicon luminosity calorimeter (SICAL), are particularly important for this analysis to veto events with detected scattered electrons. The LCAL is a lead/proportional-tube calorimeter, similar to ECAL, placed around the beam pipe at each end of the detector. It monitors angles from 45 to 160 mrad with an energy resolution of $0.15\sqrt{E(\mathrm{GeV})}$. The SICAL uses 12 silicon/tungsten layers to sample showers. It is mounted around the beam pipe in front of the LCAL, covering angles from 34 to 58 mrad, with an energy resolution of $0.225\sqrt{E(\mathrm{GeV})}$.

Table 1. Considered background processes and associated Monte Carlo generators

Process	Monte Carlo Generator
$e^+e^- \to q\bar{q}$	PYTHIA 5.7 [4]
$e^+e^- \to \tau^+\tau^-$	KORALZ 4.2 [7]
$e^+e^- \to e^+e^-\tau^+\tau^-$	PHOT02 [8]
$e^+e^- \to W^+W^-$	KORALW 1.21 [9]

The information from the tracking detectors and the calorimeters are combined in an energy-flow algorithm [3]. For each event, the algorithm provides a set of charged and neutral reconstructed particles, called *energy-flow objects*.

3 Monte Carlo simulations

In order to simulate the process

$$e^+e^- \to e^+e^-\gamma\gamma \to e^+e^-c\bar{c} \to e^+e^-D^{*\pm}X,$$

the leading-order (LO) PYTHIA 6.121 Monte Carlo [4] is used. Events are generated at e^+e^- centre-of-mass energies ranging from 183 GeV to 209 GeV using the corresponding integrated luminosities for weighting. Two different samples, direct and single-resolved processes, were generated for each of the considered D^{*+} decay modes using matrix elements for the massive charm quark. The charm quark mass m_{c} is chosen to be $1.5\,\mathrm{GeV/c^2}$ and the parameter Λ_{QCD} is set to $0.291\,\mathrm{GeV/c^2}$. The $\gamma\gamma$ invariant mass $W_{\gamma\gamma}$ is required to be at least $3.875\,\mathrm{GeV/c^2}$, which is the $D\bar{D}$ threshold. In order to ensure that both photons are quasi-real, the maximum squared four-momentum transfer Q^2_{max} is limited to $4.5\,\mathrm{GeV/c^2}$. In the single-resolved process, the SaS-1D [5] parametrization is used for the partonic distribution of the resolved photon. The Peterson et al. parametrization [6] is adopted as the fragmentation function of the charm quark with the nonperturbative parameter $\epsilon_{\mathrm{c}} = 0.031$. The background process $e^+e^- \to e^+e^-\gamma\gamma \to e^+e^-b\bar{b}$ is simulated using PYTHIA 6.121 with $W_{\gamma\gamma}$ being required to be at least $10.5\,\mathrm{GeV/c^2}$, which is the $B\bar{B}$ threshold. The b quark mass is set to $4.5\,\mathrm{GeV/c^2}$. Again the Peterson et al. parametrization is adopted with $\epsilon_{\mathrm{b}} = 0.0035$. Other possible background processes have been simulated using appropriate Monte Carlo generators as listed in Table 1.

4 Event selection and reconstruction of D^{*+} mesons

4.1 Selection of $\gamma\gamma$ events

The data analyzed were collected by the ALEPH detector at e^+e^- centre-of-mass energies ranging from 183 GeV to 209 GeV with an integrated luminosity $\mathcal{L} = 699\,\mathrm{pb^{-1}}$. The

event variables used for the event preselection are based on the ALEPH energy-flow objects. The following cuts, derived from Monte Carlo studies, were applied to select two-photon events.

- The event must contain at least 3 charged particles. This cut reduces the background from leptonic events.
- The visible invariant mass $W_{\rm vis}$ of the event must lie between $4\,\mathrm{GeV}/c^2$ and $55\,\mathrm{GeV}/c^2$ while the total energy of charged particles $E_{\rm ch}$ should not exceed 35 GeV in order to reject the e^+e^- annihilation background.
- The visible transverse momentum $p_{\rm t,vis}$ of the event is required to be less than $8\,\mathrm{GeV}/c$, as the $p_{\rm t,vis}$ distribution has a much longer tail for all considered background processes.
- To reject further background processes a cut combining the number of charged tracks and the visible energy $E_{\rm vis}$ of the event is applied: $N_{\rm ch} < 40 - \frac{2}{3}E_{\rm vis}(\mathrm{GeV})$.
- Finally, in order to retain only events with almost on-shell photons an anti-tagging condition was applied, i.e., tagged events were rejected. A tag in this analysis is defined as an energy-flow object in the luminosity calorimeters (LCAL and SICAL) with an energy of at least 30 GeV.

This selection retains a sample of 4.9 million events. Monte Carlo studies of possible background sources predict a $\gamma\gamma$ purity of 98.8%.

4.2 Reconstruction of D^{*+} mesons

Charm quarks are detected using reconstructed D^{*+} mesons which decay via $D^{*+} \to D^0\pi^+$, with the D^0 being identified in three decay modes, (1) $K^-\pi^+$, (2) $K^-\pi^+\pi^0$, and (3) $K^-\pi^+\pi^-\pi^+$. As a basis for possible $K^\pm$ and $\pi^\pm$ candidates reconstructed tracks of charged particles which fulfill the following quality conditions are used:

p	$> 100\,\mathrm{MeV}/c$	(momentum of track),
$\lvert d_0\rvert$	$< 2\,\mathrm{cm}$	(distance to beam axis at closest approach),
$\lvert z_0\rvert$	$< 8\,\mathrm{cm}$	(z coordinate at closest approach),
$N_{\rm TPC}$	≥ 4	(number of hits in TPC),
$\lvert\cos\theta\rvert$	< 0.94	(θ = polar angle with respect to beam axis).

A track surviving these cuts is classified as a kaon if the measured specific energy loss $\mathrm{d}E/\mathrm{d}x$ of the track is consistent with the expectation value for the kaon mass hypothesis, i.e., if the corresponding confidence level $P_{\rm K}$ is greater than 10%. The track is classified as a pion if P_π is at least 1%. Thus, each track can be flagged as a kaon or pion or both or neither.

The π^0 candidates are formed from pairs of photons found in ECAL with an energy of at least 250 MeV each and an invariant mass within $85\,\mathrm{MeV}/c^2$ of the nominal π^0 mass. In order to improve the energy resolution of these π^0's the energies of the photons are refitted using the π^0 mass as constraint. If the confidence level of this fit is greater than 5% and if $|\cos\theta_{\pi^0}| < 0.93$, where θ_{π^0} is the polar angle of the π^0 candidate with respect to the beam axis, the π^0 candidate is retained.

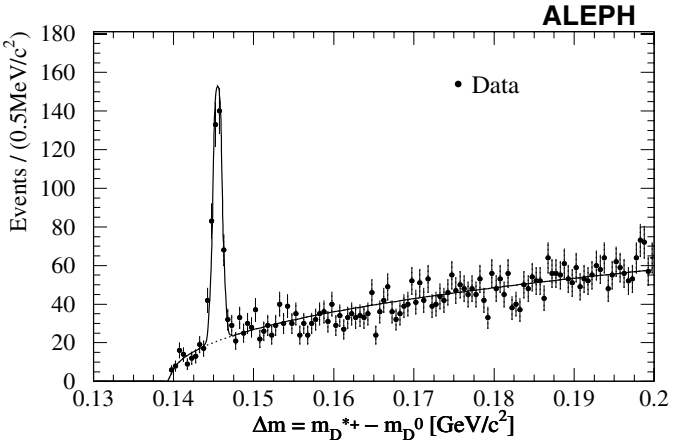

Fig. 2. Mass difference of reconstructed D^{*+} and D^0 candidates for all considered D^0 decay modes together. The points show data, the error bars represent statistical uncertainties, and the solid curve indicates the result of an unbinned maximum likelihood fit

The D^0 candidates are formed from appropriate combinations of identified kaons and pions according to three considered decay modes. The D^0 candidate is retained if it has an invariant mass within $20\,\mathrm{MeV}/c^2$, $65\,\mathrm{MeV}/c^2$, and $20\,\mathrm{MeV}/c^2$ of the nominal D^0 mass for decay mode (1), (2), and (3), respectively. These mass ranges correspond to about three times the mass resolution. In order to reduce the combinatorial background in mode (3), the four tracks composing the D^0 are fitted to a common vertex and the confidence level of this fit is required to be greater than 0.2%. The combination of each D^0 with one of the remaining π^+ candidates is considered to be a D^{*+} candidate. In order to reduce combinatorial background from soft processes and to limit the kinematic range of the D^{*+} to the acceptance range of the detector with reasonable efficiency, cuts were applied to the transverse momentum $p_{\rm t}$ and the pseudorapidity $\eta = -\ln(\tan(\theta/2))$ of the D^{*+}:

$$2\,\mathrm{GeV}/c < p_{\rm t}^{\mathrm{D}^{*+}} < 12\,\mathrm{GeV}/c\,, \quad |\eta^{\mathrm{D}^{*+}}| < 1.5 \quad . \qquad (1)$$

If there are several D^{*+} candidates found in one event the corresponding D^0 candidates are compared in mass and only the candidate with D^0 mass nearest the nominal D^0 mass is retained. If two or more D^{*+} candidates share the same D^0 candidate, all of them are retained. Figure 2 shows the mass difference $\Delta m = m_{\mathrm{D}^{*+}} - m_{\mathrm{D}^0}$ for the selected D^{*+} candidates for all three decay modes together. The spectrum rises at the lower threshold given by the pion mass. A clear peak is seen around $145.5\,\mathrm{MeV}/c^2$. In order to extract the number of D^{*+} events the data distribution is fitted with the following parametrization:

$$F(\Delta m) = N\left[\frac{1}{\sqrt{2\pi}\sigma}\exp\left\{-\frac{1}{2}\left(\frac{\Delta m - 145.5\,\mathrm{MeV}/c^2}{\sigma}\right)^2\right\}\right.$$

$$+C\,(\Delta m - m_{\pi^+})^P \Big] \quad . \tag{2}$$

In order to exclude systematic binning effects an unbinned maximum likelihood fit is performed where C and P are used as free parameters. The normalization N follows from the constraint that the integral of $F(\Delta m)$ over the range of the fit, $130\,\mathrm{MeV}/c^2 < \Delta m < 200\,\mathrm{MeV}/c^2$, must be equal to the number of entries in the histogram. The width σ of the Gaussian describing the peak is fixed to $0.5\,\mathrm{MeV}/c^2$, as determined in Monte Carlo. The number of D^{*+} events is then obtained by integrating the Gaussian part of (2) in the range of $145.5\,\mathrm{MeV}/c^2 \pm 3\sigma$. As the result a total of $360.0 \pm 27.0_{\mathrm{stat}}$ D^{*+} events are observed for all three D^{*+} decay modes together. No event contributed more than one combination to this signal region from $144\,\mathrm{MeV}/c^2$ to $147\,\mathrm{MeV}/c^2$. In the upper sideband less than 10% of the events gave two candidates, mainly in the $D^{*+} \to (K^-\pi^+\pi^-\pi^+)\pi^+$ decay channel. Among the possible background processes, only the contribution from $\gamma\gamma \to b\bar{b} \to D^{*\pm}X$ is found to be sizeable. This contribution is estimated to be $20.5 \pm 1.6_{\mathrm{stat}}$ D^{*+} events from a $\gamma\gamma \to b\bar{b} \to D^{*\pm}X$ Monte Carlo sample and the total cross section $\sigma(e^+e^- \to e^+e^-b\bar{b})$ measured in [11]. After subtraction of this background, a total of $339.5 \pm 27.0_{\mathrm{stat}}$ D^{*+} events are found in the data sample analyzed. The mass difference distributions for three channels separately are shown in Fig. 3.

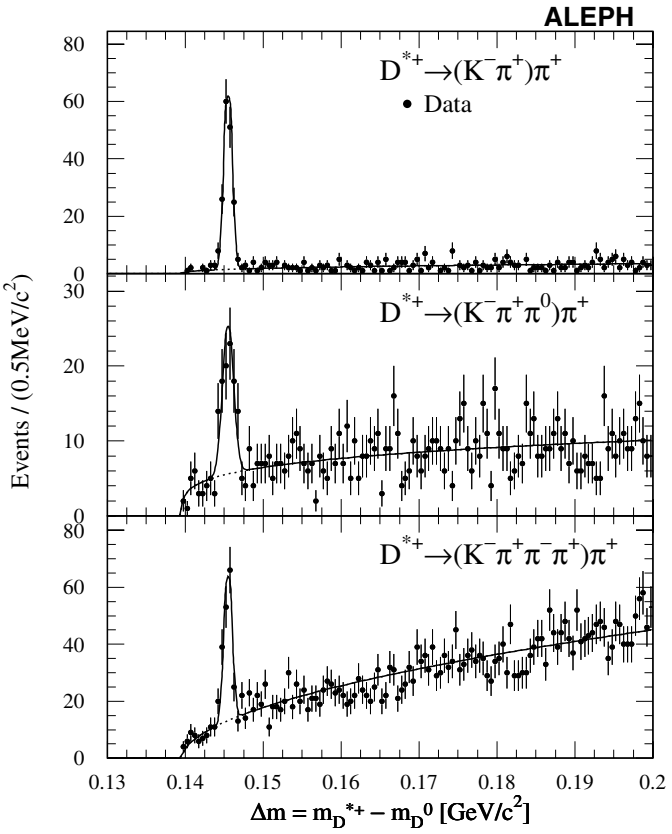

Fig. 3. Mass difference of reconstructed D^{*+} and D^0 candidates for three considered D^0 decay modes separately. The points show data, the error bars represent statistical uncertainties, and the solid curves indicate the result of unbinned likelihood fits

5 Cross section measurements

5.1 Relative fractions of direct and single-resolved contributions

As mentioned in the introduction, open charm production in $\gamma\gamma$ collisions is dominated by contributions from direct and single-resolved processes. In the direct case the $c\bar{c}$ pair makes up the final state of the $\gamma\gamma$ system (in LO) whereas in the single-resolved case the partons of the resolved photon (photon residue) in addition to the $c\bar{c}$ pair make up the final state. The transverse momentum $p_t^{D^{*+}}$ of the D^{*+} is correlated with the invariant mass of the $c\bar{c}$ system and the total visible invariant mass W_{vis} is in turn correlated with the invariant mass of the total $\gamma\gamma$ system. The ratio $p_t^{D^{*+}}/W_{\mathrm{vis}}$ should therefore be distributed at higher values for the direct case compared to the distribution of single-resolved events.

Figure 4 shows the distribution of $p_t^{D^{*+}}/W_{\mathrm{vis}}$ in data for all events found in the signal region of the mass-difference spectrum. Combinatorial background has been subtracted using events of the upper sideband $0.16\,\mathrm{GeV}/c^2 < \Delta m < 0.2\,\mathrm{GeV}/c^2$ of the mass-difference spectrum. Background from $b\bar{b}$ production has also been subtracted. The relative fractions are determined by fitting the sum of the direct and single-resolved Monte Carlo distributions to data with the relative fraction as a free parameter of the fit. The total number of entries in this Monte Carlo

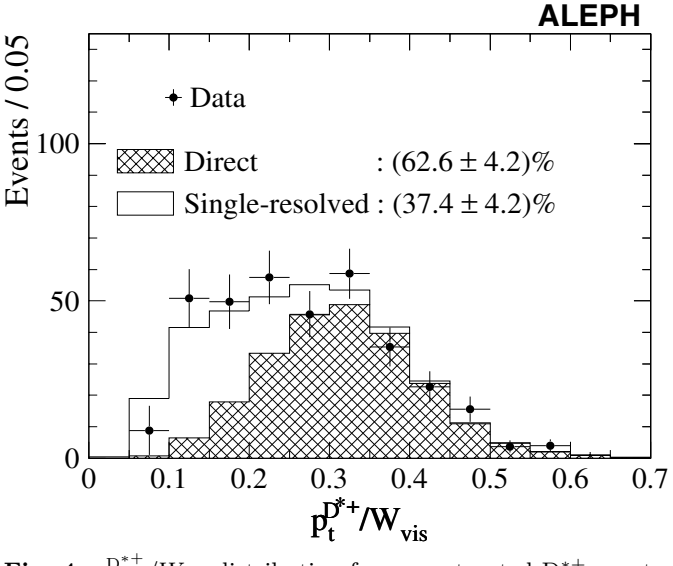

Fig. 4. $p_t^{D^{*+}}/W_{\mathrm{vis}}$ distribution for reconstructed D^{*+} events. The points with error bars show data. The relative contributions from direct (shaded histogram) and single-resolved (open histogram) processes are extracted by means of a fit

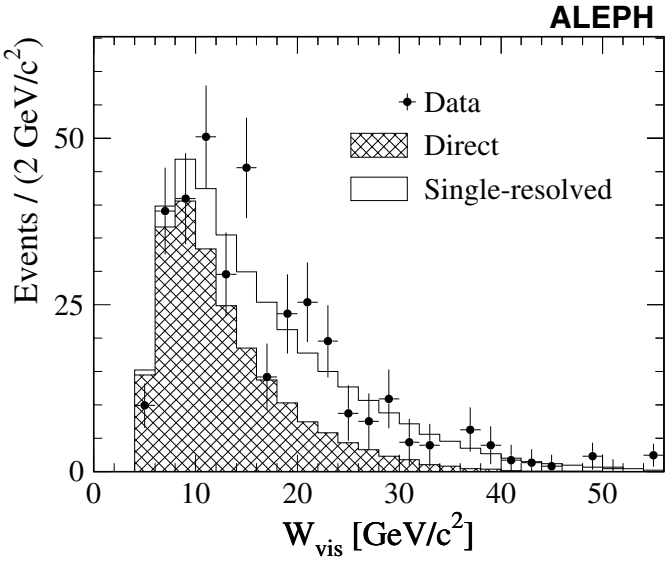

Fig. 5. The visible invariant mass $W_{\rm vis}$ distribution for reconstructed D^{*+} events. The points with error bars show data with background subtracted. The contributions from direct (shaded histogram) and single-resolved (open histogram) processes in Monte Carlo are shown according to their relative fractions determined in Sect. 5.1

sum is required to be equal to the number of entries in the data distribution. The fit yields a direct contribution of $r_{\rm dir} = (62.6 \pm 4.2)\%$ and a single-resolved contribution of $r_{\rm res} = 1 - r_{\rm dir} = (37.4 \pm 4.2)\%$. Figure 5 shows the $W_{\rm vis}$ distribution for reconstructed D^{*+} data events in comparison to that of Monte Carlo events. The contributions from direct and single-resolved processes in the Monte Carlo are added up according to their measured relative fractions. The total number of entries of this Monte Carlo sum is then normalized to the number of entries in the data distribution. The overall agreement between data and Monte Carlo is satisfactory.

5.2 Differential cross sections

Two differential cross sections for the production of D^{*+} mesons are determined: the first one as a function of the transverse D^{*+} momentum $p_{\rm t}^{D^{*+}}$, and the second as a function of pseudorapidity $|\eta^{D^{*+}}|$. Both are restricted to the range defined in (1). The former is measured in three $p_{\rm t}^{D^{*+}}$ bins: [2–3], [3–5], [5–12] GeV/c, and the latter in three $|\eta^{D^{*+}}|$ bins: [0–0.5], [0.5–1.0], [1.0–1.5]. All considered D^{*+} decay modes were treated separately.

The average differential cross section $\mathrm{d}\sigma/\mathrm{d}p_{\rm t}^{D^{*+}}$ for a given $p_{\rm t}^{D^{*+}}$ bin and $|\eta^{D^{*+}}| < 1.5$ is obtained by

$$\frac{\mathrm{d}\sigma}{\mathrm{d}p_{\rm t}^{D^{*+}}} = \frac{N_{\rm found}^{D^{*+}}}{\Delta p_{\rm t}^{D^{*+}} \mathcal{L} B_* B_0 \epsilon_{p_{\rm t}^{D^{*+}}}} \quad . \tag{3}$$

Analogously one obtains $\mathrm{d}\sigma/\mathrm{d}|\eta^{D^{*+}}|$ for a given bin in $|\eta^{D^{*+}}|$ and $2\,\mathrm{GeV}/c < p_{\rm t}^{D^{*+}} < 12\,\mathrm{GeV}/c$

$$\frac{\mathrm{d}\sigma}{\mathrm{d}|\eta^{D^{*+}}|} = \frac{N_{\rm found}^{D^{*+}}}{\Delta|\eta^{D^{*+}}| \mathcal{L} B_* B_0 \epsilon_{|\eta^{D^{*+}}|}} \quad ,$$

where

- $N_{\rm found}^{D^{*+}}$ is the number of D^{*+} found in the considered bin after subtracting the $b\bar{b}$ background (determined as described in Sect. 4.2) with the width of the fitted Gaussian (2) being fixed to $0.5\,\mathrm{MeV}/c^2$ for decay modes (1) and (3) and $0.7\,\mathrm{MeV}/c^2$ for decay mode (2),
- $\Delta p_{\rm t}^{D^{*+}}$, $\Delta|\eta^{D^{*+}}|$ are the considered intervals in $p_{\rm t}^{D^{*+}}$ and $|\eta^{D^{*+}}|$,
- $\mathcal{L} = 699\,\mathrm{pb}^{-1}$ is the integrated luminosity of the data analyzed,
- B_* is the branching ratio $\mathrm{BR}(D^{*+} \to D^0\pi^+) = (68.3 \pm 1.4)\%$ [10],
- B_0 is the branching ratio of the considered D^0 decay mode [10],
- $\epsilon_{p_{\rm t}^{D^{*+}}}$ ($\epsilon_{|\eta^{D^{*+}}|}$) is the efficiency of reconstructing a D^{*+} candidate in the given $p_{\rm t}^{D^{*+}}$ ($|\eta^{D^{*+}}|$) bin in the considered decay mode. Since efficiencies are determined separately for direct and single-resolved processes ($\epsilon^{\rm dir}_{p_{\rm t}^{D^{*+}}}$ and $\epsilon^{\rm res}_{p_{\rm t}^{D^{*+}}}$, respectively) the total efficiency is a weighted combination using the fractions as determined in Sect. 5.1,

$$\epsilon_{p_{\rm t}^{D^{*+}}} = r_{\rm dir}\epsilon^{\rm dir}_{p_{\rm t}^{D^{*+}}} + r_{\rm res}\epsilon^{\rm res}_{p_{\rm t}^{D^{*+}}} \quad ,$$
$$\epsilon_{|\eta^{D^{*+}}|} = r_{\rm dir}\epsilon^{\rm dir}_{|\eta^{D^{*+}}|} + r_{\rm res}\epsilon^{\rm res}_{|\eta^{D^{*+}}|} \quad .$$

Tables 2 and 3 show the number of D^{*+} mesons found in the chosen $p_{\rm t}^{D^{*+}}$ and $|\eta^{D^{*+}}|$ bins respectively, as well as the derived differential cross sections $\mathrm{d}\sigma/\mathrm{d}p_{\rm t}^{D^{*+}}$ and $\mathrm{d}\sigma/\mathrm{d}|\eta^{D^{*+}}|$ with their statistical and systematic errors. The resulting cross sections for the different D^{*+} decay modes are consistent with each other for all bins in $p_{\rm t}^{D^{*+}}$ as well as in $|\eta^{D^{*+}}|$, taking into account the statistical uncertainties. The weighted average over all of the considered D^{*+} decay modes is given in Table 4 for each $p_{\rm t}^{D^{*+}}$ and $|\eta^{D^{*+}}|$ bin, where only the dominating statistical uncertainties are used for weighting.

5.2.1 Systematic errors on differential cross sections

The study of systematic errors was performed separately for each $p_{\rm t}^{D^{*+}}$ and $|\eta^{D^{*+}}|$ bin and for each of the considered D^{*+} decay modes, unless otherwise specified.

The systematic error introduced by the event selection was studied by varying the cuts within the resolution obtained from the Monte Carlo detector simulation. The systematic uncertainty was estimated from the resulting

Table 2. The numbers of D^{*+} mesons found with $|\eta^{D^{*+}}| < 1.5$ in bins of $p_t^{D^{*+}}$ for the three decay modes after background subtraction. The efficiency is listed separately for direct and single-resolved processes. The differential cross section in bins of the transverse momentum $p_t^{D^{*+}}$ of the D^{*+} for each considered D^{*+} decay mode is given together with statistical and systematic errors

$p_t^{D^{*+}}$ range	$N_{found}^{D^{*+}}$		
[GeV/c]	$D^{*+} \to (K^-\pi^+)\pi^+$	$D^{*+} \to (K^-\pi^+\pi^0)\pi^+$	$D^{*+} \to (K^-\pi^+\pi^-\pi^+)\pi^+$
2–3	69.8 ± 10.7	18.7 ± 6.2	54.5 ± 10.3
3–5	72.2 ± 8.1	29.0 ± 7.8	44.9 ± 9.7
5–12	15.1 ± 3.0	20.9 ± 5.7	29.2 ± 6.8
	Efficiency for direct process $\epsilon^{dir}_{p_t^{D^{*+}}}$ (%)		
	$D^{*+} \to (K^-\pi^+)\pi^+$	$D^{*+} \to (K^-\pi^+\pi^0)\pi^+$	$D^{*+} \to (K^-\pi^+\pi^-\pi^+)\pi^+$
2–3	27.96 ± 0.13	2.27 ± 0.04	11.66 ± 0.09
3–5	46.94 ± 0.20	6.83 ± 0.10	24.16 ± 0.17
5–12	48.73 ± 0.34	12.32 ± 0.23	30.13 ± 0.33
	Efficiency for single-resolved process $\epsilon^{res}_{p_t^{D^{*+}}}$ (%)		
	$D^{*+} \to (K^-\pi^+)\pi^+$	$D^{*+} \to (K^-\pi^+\pi^0)\pi^+$	$D^{*+} \to (K^-\pi^+\pi^-\pi^+)\pi^+$
2–3	26.81 ± 0.12	2.12 ± 0.04	10.49 ± 0.09
3–5	41.95 ± 0.21	6.17 ± 0.10	20.78 ± 0.18
5–12	34.59 ± 0.41	8.8 ± 0.24	19.83 ± 0.36
	$d\sigma/dp_t^{D^{*+}}$ (pb/GeV/c)		
	$D^{*+} \to (K^-\pi^+)\pi^+$	$D^{*+} \to (K^-\pi^+\pi^0)\pi^+$	$D^{*+} \to (K^-\pi^+\pi^-\pi^+)\pi^+$
2–3	$13.80 \pm 2.12 \pm 1.04$	$12.70 \pm 4.21 \pm 1.20$	$13.38 \pm 2.51 \pm 0.89$
3–5	$4.36 \pm 0.49 \pm 0.22$	$3.32 \pm 0.90 \pm 0.27$	$2.70 \pm 0.58 \pm 0.17$
5–12	$0.27 \pm 0.05 \pm 0.01$	$0.41 \pm 0.11 \pm 0.03$	$0.44 \pm 0.10 \pm 0.03$

relative variation of the efficiency. This yields an uncertainty of 0.6%–6.4%, depending on the considered $p_t^{D^{*+}}$ or $|\eta^{D^{*+}}|$ bin and on the D^{*+} decay mode.

The selection of pion and kaon candidates depends essentially on the dE/dx measurement as well as on the expectation values $dE/dx_{exp,h}$ used to calculate the probability for a given mass hypothesis m_h. The uncertainty of the dE/dx calibration changes the efficiency by 0.5%–5.8%. These deviations are used as an estimate of the systematic error.

The systematic error due to the accepted mass range used to classify D^0 candidates was examined by comparison of the mass distributions of D^0 candidates which contributed to the D^{*+} signal in data and Monte Carlo for each D^0 decay mode separately. A Gaussian fit was applied to these distributions. The fraction of the fitted Gaussian which lies within the accepted mass range differs between data and Monte Carlo by less than 0.6%. Thus, the uncertainty due to this source can be neglected.

In order to estimate the error introduced by the method for extracting the number of D^{*+} events (Sect. 4.2) the mean of the fitted Gaussian in (2) was varied by $\pm 0.05\,\mathrm{MeV}/c^2$, and the width was varied by 10% about its values as obtained in Monte Carlo. The resulting relative error on the efficiencies was 0.8%–2.1%.

A variation of the interval that defines the upper sideband yields a variation in r_{dir} of less than 0.05%. Hence, this source is negligible. The present analysis assumes the fraction r_{dir} to be constant over the considered kinematic range. Monte Carlo studies show a variation of this fraction of up to 12% in this range, depending on the bin in $p_t^{D^{*+}}$ and $|\eta^{D^{*+}}|$. A relative uncertainty of 10% is therefore added in quadrature to the statistical uncertainty of r_{res}. A variation of $r_{dir/res}$ within these uncertainties yields a variation in the cross section of 0.3%–3.4%, which is used to estimate the introduced uncertainty.

The statistical error of $b\bar{b}$ background subtraction and the uncertainties of the total cross section $\sigma(e^+e^- \to e^+e^- b\bar{b})$ yield a systematic error of 1.2%–3.4% on the differential cross sections.

The overall trigger efficiency of the selected D^{*+} events is estimated to be consistent with 100% with a statistical uncertainty of 1%. Thus no correction is made for this source.

The relative errors on the branching ratios given in [10] are used to estimate the corresponding relative systematic uncertainties in the cross sections.

Similarly the relative uncertainties in the efficiencies due to finite statistics in the Monte Carlo samples, 0.5%–2.3%, are taken into account.

Table 3. The numbers of D^{*+} mesons found with $2\,\mathrm{GeV}/c < p_t^{D^{*+}} < 12\,\mathrm{GeV}/c$ in bins of $|\eta^{D^{*+}}|$ for the three decay modes after background subtraction. The efficiency is listed separately for direct and single-resolved processes. The differential cross section in bins of the pseudorapidity $|\eta^{D^{*+}}|$ of the D^{*+} for each considered D^{*+} decay mode is given together with statistical and systematic errors

$\eta^{D^{*+}}$ range	$N_{\mathrm{found}}^{D^{*+}}$		
	$D^{*+} \to (K^-\pi^+)\pi^+$	$D^{*+} \to (K^-\pi^+\pi^0)\pi^+$	$D^{*+} \to (K^-\pi^+\pi^-\pi^+)\pi^+$
0.0–0.5	49.2 ± 8.9	21.8 ± 6.8	51.1 ± 10.0
0.5–1.0	50.8 ± 8.3	26.4 ± 7.6	45.8 ± 9.5
1.0–1.5	56.4 ± 7.9	18.5 ± 6.3	29.3 ± 7.6
	Efficiency for direct process $\epsilon^{\mathrm{dir}}_{\lvert\eta^{D^{*+}}\rvert}(\%)$		
	$D^{*+} \to (K^-\pi^+)\pi^+$	$D^{*+} \to (K^-\pi^+\pi^0)\pi^+$	$D^{*+} \to (K^-\pi^+\pi^-\pi^+)\pi^+$
0.0–0.5	41.71 ± 0.19	5.45 ± 0.09	20.90 ± 0.16
0.5–1.0	39.07 ± 0.19	5.24 ± 0.08	19.70 ± 0.16
1.0–1.5	27.88 ± 0.17	3.72 ± 0.07	12.19 ± 0.13
	Efficiency for single-resolved process $\epsilon^{\mathrm{res}}_{\lvert\eta^{D^{*+}}\rvert}(\%)$		
	$D^{*+} \to (K^-\pi^+)\pi^+$	$D^{*+} \to (K^-\pi^+\pi^0)\pi^+$	$D^{*+} \to (K^-\pi^+\pi^-\pi^+)\pi^+$
0.0–0.5	37.55 ± 0.20	4.53 ± 0.08	17.31 ± 0.16
0.5–1.0	34.74 ± 0.19	4.16 ± 0.08	15.95 ± 0.15
1.0–1.5	24.08 ± 0.16	2.75 ± 0.06	9.66 ± 0.11
	$\mathrm{d}\sigma/\mathrm{d}\lvert\eta^{D^{*+}}\rvert\,[\mathrm{pb}]$		
	$D^{*+} \to (K^-\pi^+)\pi^+$	$D^{*+} \to (K^-\pi^+\pi^0)\pi^+$	$D^{*+} \to (K^-\pi^+\pi^-\pi^+)\pi^+$
0.0–0.5	$13.33 \pm 2.40 \pm 0.85$	$12.86 \pm 4.02 \pm 1.10$	$14.40 \pm 2.80 \pm 1.00$
0.5–1.0	$14.78 \pm 2.40 \pm 0.86$	$16.48 \pm 4.75 \pm 1.36$	$13.81 \pm 2.87 \pm 0.91$
1.0–1.5	$23.22 \pm 3.24 \pm 2.10$	$16.59 \pm 5.63 \pm 1.73$	$14.35 \pm 3.70 \pm 1.31$

Table 4. The combined differential cross sections, $\mathrm{d}\sigma/\mathrm{d}p_t^{D^{*+}}$ and $\mathrm{d}\sigma/\mathrm{d}|\eta^{D^{*+}}|$

	$p_t^{D^{*+}}$ range [GeV/c]		
	2–3	3–5	5–12
$\mathrm{d}\sigma/\mathrm{d}p_t^{D^{*+}}$ [pb/(GeV/c)]	$13.50 \pm 1.51 \pm 1.01$	$3.61 \pm 0.34 \pm 0.21$	$0.32 \pm 0.04 \pm 0.02$
	$\lvert\eta^{D^{*+}}\rvert$ range		
	0.0–0.5	0.5–1.0	1.0–1.5
$\mathrm{d}\sigma/\mathrm{d}\lvert\eta^{D^{*+}}\rvert\,[\mathrm{pb}]$	$13.62 \pm 1.65 \pm 0.94$	$14.65 \pm 1.71 \pm 0.94$	$18.93 \pm 2.23 \pm 1.75$

All systematic errors are assumed to be uncorrelated and therefore added in quadrature. Table 5 shows a summary of the systematic uncertainties.

5.2.2 Comparison to theory

Figures 6 and 7 show the measured $\mathrm{d}\sigma/\mathrm{d}p_t^{D^{*+}}$ and $\mathrm{d}\sigma/\mathrm{d}|\eta^{D^{*+}}|$ in comparison to two different NLO perturbative QCD calculations, the fixed-order (FO) NLO (also known as massive approach) [12] and the resummed (RES) NLO (massless approach) [13]. In both cases, the charm quark mass m_c is set to $1.5\,\mathrm{GeV}/c^2$, the renormalization scale μ_R and the factorization scale μ_F are chosen such that $\mu_F^2 = 4\mu_R^2 = m_T^2 \equiv m_c^2 + p_t(c)^2$, where $p_t(c)$ is the transverse momentum of the charm quark. For the resolved contribution the photonic parton densities of the GRS-HO parametrization are chosen [14] in the FO NLO calculation, whereas the RES NLO uses GRV-HO [15]. The fragmentation of the charm quark to the D^{*+} is modelled by the fragmentation function suggested by Peterson et al. [6], with $\epsilon_c = 0.035$ in the case of FO NLO. The RES NLO calculation uses $\epsilon_c = 0.185$, which was determined by using nonperturbative fragmentation functions fitted [13] to ALEPH measurements of inclusive D^{*+} produc-

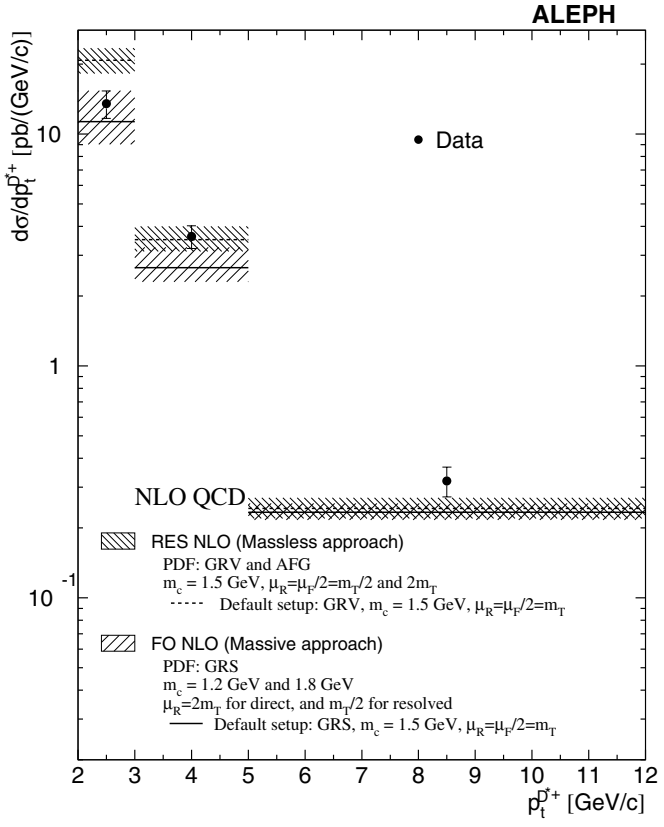

Fig. 6. Differential cross section $\mathrm{d}\sigma/\mathrm{d}p_{\mathrm{t}}^{\mathrm{D}^{*+}}$ for the inclusive D^{*+} production. The points show the combined differential cross sections from the three decay modes under studies. The error bars correspond to the quadratic sum of statistical and systematic uncertainties. The data are compared to the fixed-order (FO) NLO [12] and the resummed (RES) NLO [13] calculations shown as the solid and dashed lines, respectively. The shaded bands represent the theoretical uncertainties of these calculations

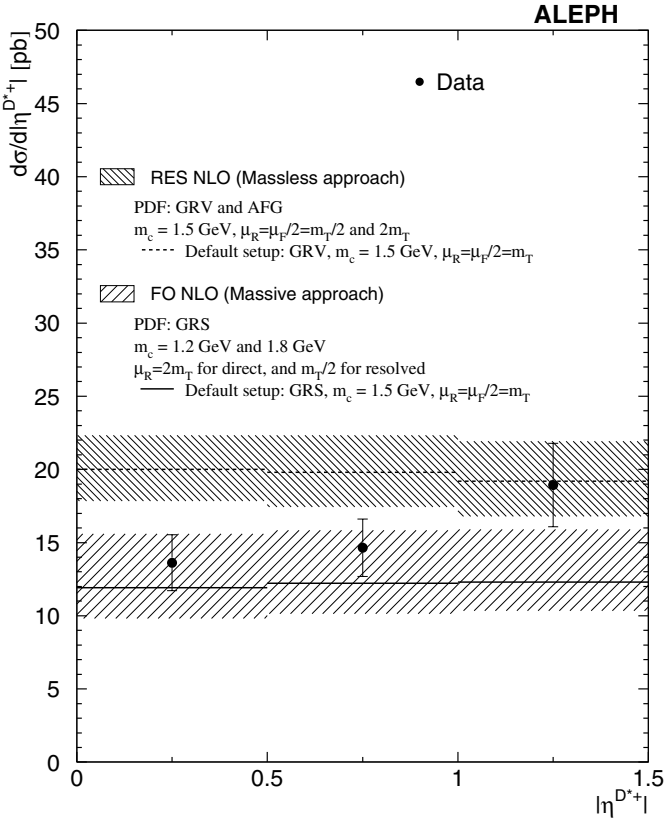

Fig. 7. Differential cross section $\mathrm{d}\sigma/\mathrm{d}|\eta^{\mathrm{D}^{*+}}|$ for the inclusive D^{*+} production. The points show the combined differential cross sections from the three decay modes under studies. The error bars correspond to the quadratic sum of statistical and systematic uncertainties. The data are compared to the fixed-order (FO) NLO [12] and the resummed (RES) NLO [13] calculations shown as the solid and dashed lines, respectively. The shaded bands represent the theoretical uncertainties of these calculations

tion in $\mathrm{e^+e^-}$ annihilation [16]. The results of the two NLO QCD calculations are represented by the dashed lines (for RES NLO) and solid lines (FO NLO) in both Fig. 6 and Fig. 7. In order to estimate the theoretical uncertainties, the FO NLO calculation was repeated with the charm mass and the renormalization scale varied as described in the figures. The RES NLO calculation is also repeated using the AFG [17] ansatz as an alternative for parton density function and varying the renormalization and factorization scales. The resulting theoretical uncertainties are indicated by the bands around the corresponding default values in Figs. 6 and 7.

Altogether, the measurement of $\mathrm{d}\sigma/\mathrm{d}p_{\mathrm{t}}^{\mathrm{D}^{*+}}$ seems to favour a harder $p_{\mathrm{t}}^{\mathrm{D}^{*+}}$ spectrum than predicted. The RES NLO calculation clearly overestimates the measurement in the low $p_{\mathrm{t}}^{\mathrm{D}^{*+}}$ region, while the FO NLO calculation slightly underestimates it in the $p_{\mathrm{t}}^{\mathrm{D}^{*+}} > 3.0\,\mathrm{GeV}/c$ region. The measured $\mathrm{d}\sigma/\mathrm{d}|\eta^{\mathrm{D}^{*+}}|$ is consistent with the almost flat distribution predicted by both NLO calculations, but the measurement of $\mathrm{d}\sigma/\mathrm{d}|\eta^{\mathrm{D}^{*+}}|$ is again overestimated by the RES NLO calculation and somewhat underestimated by the FO NLO calculation.

5.3 Visible cross section

The visible cross section $\sigma_{\mathrm{vis}}^{\mathrm{D}^{*+}}(\mathrm{e^+e^-} \to \mathrm{e^+e^-D^{*+}}X)$ is calculated separately in the acceptance range (1) for the three considered decay modes by

$$\sigma_{\mathrm{vis}}^{\mathrm{D}^{*+}}(\mathrm{e^+e^-} \to \mathrm{e^+e^-D^{*+}}X) = \frac{N_{\mathrm{found}}^{\mathrm{D}^{*+}}}{\mathcal{L}B_*B_0\epsilon} \quad , \qquad (4)$$

where the notation is as the same as in (3). The numbers of D^{*+} found and the efficiencies of reconstructing a D^{*+} candidate for direct and single-resolved processes are listed in Table 6 together with the derived visible cross sections $\sigma_{\mathrm{vis}}^{\mathrm{D}^{*+}}(\mathrm{e^+e^-} \to \mathrm{e^+e^-D^{*+}}X)$ and their uncertainties for the three decay modes. The systematic error is determined in the same way as for differential cross sections (Sect. 5.2.1). The weighted average over all of the

Table 5. Sources of systematic uncertainty on the differential cross sections

Source	Estimated uncertainty
Event selection	(0.6–6.4)%
K/π selection	(0.5–5.7)%
Accepted mass range for D^0	< 0.16%, neglected
D^{*+} selection	(0.8–2.1)%
D^{*+} from annihilation events	< 1%, neglected
$b\bar{b}$ background subtraction	(1.2–3.4)%
Fraction of direct/resolved $r_{\mathrm{dir}}/r_{\mathrm{res}}$	(0.3–3.4)%
$BR(D^{*+} \to D^0\pi^+)$	2.0%
$BR(D^0 \to K^-\pi^+)$	2.3%
$BR(D^0 \to K^-\pi^+\pi^0)$	6.5%
$BR(D^0 \to K^-\pi^+\pi^-\pi^+)$	5.3%
Statistical limitation in Monte Carlo	(0.5–2.3)%

considered decay modes using the dominating statistical uncertainties for weighting is

$$\sigma_{\mathrm{vis}}^{\mathrm{D}^{*+}}(\mathrm{e^+e^-} \to \mathrm{e^+e^-D^{*+}}X) = 23.39 \pm 1.64_{\mathrm{stat}} \pm 1.52_{\mathrm{syst}}\ \mathrm{pb} \quad . \tag{5}$$

The cross section theoretically predicted by the FO NLO calculation [12] is

$$\sigma_{\mathrm{vis}}^{\mathrm{D}^{*+}}(\mathrm{e^+e^-} \to \mathrm{e^+e^-D^{*+}}X) = 17.3^{+5.1}_{-2.9}\ \mathrm{pb} \quad , \tag{6}$$

and is consistent with this measurement within the given uncertainties.

5.4 Total cross section

The total cross section for the reaction $\mathrm{e^+e^-} \to \mathrm{e^+e^-c\bar{c}}$ is given by

$$\sigma(\mathrm{e^+e^-} \to \mathrm{e^+e^-c\bar{c}}) = \frac{\sigma_{\mathrm{vis}}^{\mathrm{D}^{*+}}}{2P_{\mathrm{c}\to\mathrm{D}^{*+}}}(r_{\mathrm{dir}}R_{\mathrm{dir}} + r_{\mathrm{res}}R_{\mathrm{res}}) \quad , \tag{7}$$

where the symbols are as follows:

- $\sigma_{\mathrm{vis}}^{\mathrm{D}^{*+}}$ is the visible inclusive D^{*+} cross section determined in the previous section;
- $P_{\mathrm{c}\to\mathrm{D}^{*+}}$ is the probability for a charm quark to fragment into a D^{*+} meson (taking the combined quantity $P_{\mathrm{c}\to\mathrm{D}^{*+}} \times BR(D^{*+} \to D^0\pi^+) = 0.1631 \pm 0.0050$ from [18] and using $BR(D^{*+} \to D^0\pi^+) = (68.3 \pm 1.4)$% [10] yields $P_{\mathrm{c}\to\mathrm{D}^{*+}} = 0.2388 \pm 0.0088$);
- the factor 2 in the denominator takes into account that, for the single inclusive cross sections, both the D^{*+} and the D^{*-} mesons were counted;
- r_{dir} and r_{res} are the fractions of the direct and single-resolved contributions in the considered acceptance range, as described in Sect. 5.1;
- R_{dir} is the ratio

$$R_{\mathrm{dir}} = \frac{\sigma_{\mathrm{tot,dir}}^{\mathrm{D}^{*+}}}{\sigma_{\mathrm{vis,dir}}^{\mathrm{D}^{*+}}}$$

of the total D^{*+} cross section to the visible cross section in the range of (1) for direct processes. It describes the extrapolation of the measured cross section to the total phase space available. R_{res} is the corresponding quantity for the single-resolved case.

Separate Monte Carlo samples are used to estimate R_{dir} and R_{res} for direct and single-resolved processes. The parameters used to determine R_{dir} and R_{res} are described in Sect. 3. This yields $R_{\mathrm{dir}} = 12.74 \pm 0.45_{\mathrm{stat}}$ and $R_{\mathrm{res}} = 18.62 \pm 0.80_{\mathrm{stat}}$.

The main theoretical uncertainties entering the calculation of the extrapolation factors stem from the uncertainty of the charm quark mass. A variation of the charm mass to $m_{\mathrm{c}} = 1.3\,\mathrm{GeV}/c^2$ and $m_{\mathrm{c}} = 1.7\,\mathrm{GeV}/c^2$ yields relative errors on R_{dir} of ± 10% and on R_{res} of $+43$% and -19%, respectively.

In the single-resolved case an additional uncertainty enters R_{res} by the choice of the parton density functions describing the resolved photon. Alternatively to the default choice the GRV-LO parametrization [19] was used to calculate R_{res}. This yields a relative deviation of 12% and is added in quadrature to the other systematic uncertainties on R_{res}. The following values are therefore obtained:

$$R_{\mathrm{dir}} = 12.7 \pm 1.3$$
$$R_{\mathrm{res}} = 18.6^{+8.3}_{-4.2} \quad .$$

The uncertainties in r_{dir}, $\sigma_{\mathrm{vis}}^{\mathrm{D}^{*+}}$, and $P_{\mathrm{c}\to\mathrm{D}^{*+}}$, which are assumed to be uncorrelated, are taken into account in the estimation of the statistical and systematic error on the total cross section by Gaussian error propagation. This procedure yields a total cross section for the reaction $\mathrm{e^+e^-} \to \mathrm{e^+e^-c\bar{c}}$ at $\mathrm{e^+e^-}$ centre-of-mass energies $\sqrt{s} = (183-209)\,\mathrm{GeV}$, corresponding to the luminosity weighted average of 197 GeV,

$$\sigma(\mathrm{e^+e^-} \to \mathrm{e^+e^-c\bar{c}})_{\langle\sqrt{s}\rangle=197\,\mathrm{GeV}} = 731 \pm 74_{\mathrm{stat}} \pm 47_{\mathrm{syst}}{}^{+157}_{-86_{\mathrm{extr}}}\ \mathrm{pb} \quad . \tag{8}$$

Alternatively, the total cross section is determined by means of the NLO calculation referenced in the previous section; in this case the cross section is given by

$$\sigma(\mathrm{e^+e^-} \to \mathrm{e^+e^-c\bar{c}}) = \frac{\sigma_{\mathrm{vis}}^{\mathrm{D}^{*+}}}{2P_{\mathrm{c}\to\mathrm{D}^{*+}}}R_{\mathrm{tot}} \quad . \tag{9}$$

The value $R_{\mathrm{tot}} = 22.2^{+16.0}_{-7.3}$ is extracted from [12] by determining the ratio of the calculated total charm cross section to the charm cross section calculated for the visible D^{*+} range considered in the present analysis. The large uncertainty of R_{tot} is mainly due to the uncertainty of the charm quark mass chosen in the range from $m_{\mathrm{c}} = 1.2\,\mathrm{GeV}/c^2$ to $m_{\mathrm{c}} = 1.8\,\mathrm{GeV}/c^2$. This results in a total cross section

$$\sigma(\mathrm{e^+e^-} \to \mathrm{e^+e^-c\bar{c}})_{\langle\sqrt{s}\rangle=197\,\mathrm{GeV}} = 1087 \pm 86_{\mathrm{stat}} \pm 70_{\mathrm{syst}}{}^{+783}_{-357_{\mathrm{extr}}}\ \mathrm{pb} \quad . \tag{10}$$

Table 6. The numbers of D^{*+} mesons found in the acceptance range $2\,\mathrm{GeV}/c < p_t^{D^{*+}} < 12\,\mathrm{GeV}/c$ and $|\eta^{D^{*+}}| < 1.5$ for the three decay modes after background subtraction. The efficiency is listed separately for direct and single-resolved process. The visible cross section $\sigma_{vis}^{D^{*+}}$ for each considered D^{*+} decay mode is given together with statistical and systematic errors

	$(K^-\pi^+)\pi^+$	$(K^-\pi^+\pi^0)\pi^+$	$(K^-\pi^+\pi^-\pi^+)\pi^+$
$N_{found}^{D^{*+}}$	156.4 ± 14.9	67.4 ± 12.3	128.4 ± 16.3
$\epsilon_{dir}(\%)$	36.47 ± 0.1	4.81 ± 0.05	17.71 ± 0.09
$\epsilon_{res}(\%)$	31.68 ± 0.1	3.76 ± 0.04	14.07 ± 0.08
$\sigma_{vis}^{D^{*+}}$ (pb)	$24.68 \pm 2.35 \pm 1.47$	$23.04 \pm 4.21 \pm 1.91$	$21.76 \pm 2.76 \pm 1.41$

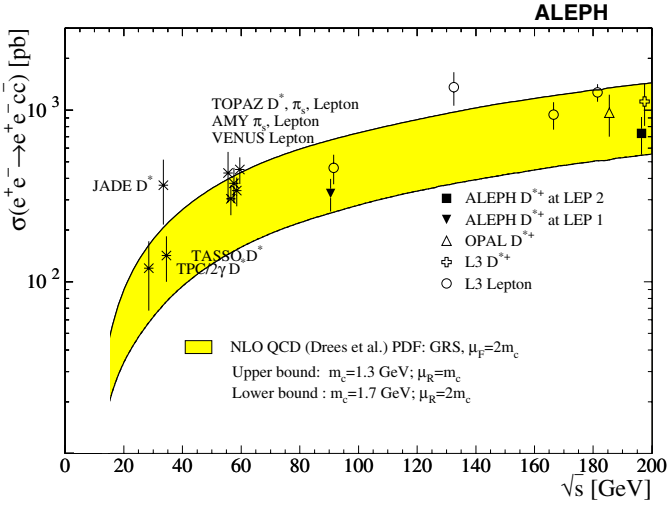

Fig. 8. The total cross section for charm production $\sigma(e^+e^- \to e^+e^-c\bar{c})$ versus the centre-of-mass energy $\sqrt{s}$ of the e^+e^- system. The measurement of this analysis is shown as a square. The band represents the NLO QCD calculation [1]. The results obtained by L3 and OPAL using D^{*+} are represented in [21] and [20], respectively. The L3 measurements using lepton tag can be found in [22]. The values for TASSO, TPC/2γ, JADE, AMY, and VENUS are taken from [23]

The measured total cross section (8) is shown in Fig. 8 in comparison to the NLO QCD prediction of Drees et al. [1] and to results from other experiments [20–23]. Within the uncertainties, this NLO QCD prediction is in good agreement with our measurement and others [24].

6 Conclusions

The inclusive production of D^{*+} mesons in two-photon collisions was measured using the ALEPH detector at LEP 2 energies in the reaction $D^{*+} \to D^0\pi^+$. The D^0 mesons were identified in the decay modes $K^-\pi^+$, $K^-\pi^+\pi^0$, and $K^-\pi^+\pi^-\pi^+$. A total of 339.5 ± 27.0 D^{*+} events from $\gamma\gamma \to c\bar{c}$ was found in the kinematic region $2\,\mathrm{GeV}/c < p_t^{D^{*+}} < 12\,\mathrm{GeV}/c$ and $|\eta^{D^{*+}}| < 1.5$.

The fractions of the main contributing processes, direct and single-resolved, were determined using the event variable $p_t^{D^{*+}}/W_{vis}$ to be $r_{dir} = (62.6 \pm 4.2)\%$ and $r_{res} = 1 - r_{dir} = (37.4 \pm 4.2)\%$, within the acceptance.

The differential cross sections $d\sigma/dp_t^{D^{*+}}$ and $d\sigma/d|\eta^{D^{*+}}|$ were measured and compared to the fixed-order (FO) NLO QCD calculation [12] and the resummed (RES) NLO QCD calculation [13]. While the data show a slightly harder spectrum in the $p_t^{D^{*+}}$ distribution compared to both calculations, the almost flat distribution of $d\sigma/d|\eta^{D^{*+}}|$ which is predicted by the NLO calculations for the visible D^{*+} region is in agreement with the measurement. Overall, the measurements of $d\sigma/dp_t^{D^{*+}}$ and $d\sigma/d|\eta^{D^{*+}}|$ were slightly underestimated by the FO NLO calculation with $m_c = 1.5\,\mathrm{GeV}/c^2$ and overestimated by the RES NLO calculation.

For the integrated visible D^{*+} cross section a value of $\sigma_{vis}^{D^{*+}} = 23.39 \pm 1.64_{stat} \pm 1.52_{syst}$ pb is obtained which is consistent with the FO NLO calculation.

The extrapolation of the visible D^{*+} cross section to the total cross section of charm production introduces large theoretical uncertainties, of which the uncertainty of the charm quark mass and the choice of parton density functions used to describe the resolved photon are the main sources. Using the LO calculation of the PYTHIA Monte Carlo we obtain

$$\sigma(e^+e^- \to e^+e^-c\bar{c})_{\langle\sqrt{s}\rangle=197\,\mathrm{GeV}} = 731 \pm 74_{stat} \pm 47_{syst} \,^{+157}_{-86_{extr}} \text{ pb} \quad .$$

A different method using the results from the FO NLO calculation [12] yields a higher cross section and a larger error.

Acknowledgements. We wish to thank our colleagues in the CERN accelerator divisions for the successful operation of LEP. We are indebted to the engineers and technicians in all our institutions for their contribution to the excellent performance of ALEPH. Those of us from non-member countries thank CERN for its hospitality. We would like to thank Stefano Frixione and Bernd Kniehl for fruitful discussions.

References

1. M. Drees, M. Krämer, J. Zunft, P. M. Zerwas, Phys. Lett. B **306**, 371 (1993)
2. ALEPH Collaboration, ALEPH: A Detector for Electron-Positron Annihilations at LEP, Nucl. Instrum. Meth. A **294**, 121 (1990); The Design, Construction and Performance of the ALEPH Silicon Vertex Detector, Nucl. Instrum. and Methods A **379** (1996) 121
3. ALEPH Collaboration, Performance of the ALEPH Detector at LEP, Nucl. Instrum. Meth. A **360**, 481 (1995)
4. T. Sjöstrand, Comput. Phys. Commun. **82**, 74 (1994)
5. G. A. Schuler, T. Sjöstrand, Z. Phys. C **68**, 607 (1995)
6. C. Peterson, D. Schlatter, I. Schmitt, P. Zerwas, Phys. Rev. D **27**, 105 (1983)
7. S. Jadach, B.F.L. Ward, Z. Wąs, The Monte Carlo program KORALZ, version 4.0, for the lepton or quark pair production at LEP / SLC energies, Comput. Phys. Commun. **79**, 503 (1994)
8. J.A.M. Vermaseren,Two Photon Processes at very high-energies, Nucl. Phys. B **229**, 347 (1983)
9. S. Jadach, M. Skrzypek, W. Placzek, Z. Wąs, Comput. Phys. Commun. **94**, 216 (1996)
10. Particle Data Group, Review of Particle Physics, Eur. Phys. J. C **15**, 1 (2000)
11. The L3 Collaboration, M. Acciarri et al., Phys. Lett. B **503**, 10 (2001)
12. S. Frixione, M. Krämer, E. Laenen, Nucl. Phys. B **571**, 169 (2000)
13. J. Binnewies, B.A. Kniehl, G. Kramer, Phys. Rev. D **58**, 014014 (1998); D **53**, 6110 (1996)
14. M. Glück, E. Reya, I. Schienbein, Phys. Rev. D **60**, 54019 (1999)
15. M. Glück, E. Reya, A. Vogt, Phys. Rev. D **46**, 1973 (1992)
16. ALEPH Collaboration, Study of charm production in Z decays, Eur. Phys. J. C **16**, 597 (2000)
17. P. Aurenche, J.P. Guillet, M. Fontannaz, Z. Phys. C **64**, 621 (1994)
18. The LEP Collaborations ALEPH, DELPHI, L3, OPAL, the LEP Electroweak Working Group and the SLD Heavy Flavour and Electroweak Groups, CERN-EP/2001-021
19. M. Glück, E. Reya, A. Vogt, Phys. Rev. D **45**, 3986 (1992)
20. The OPAL Collaboration, G. Abbiendi et al., Eur. Phys. J. C **16**, 579 (2000)
21. The L3 Collaboration, P. Achard et al., CERN-EP/2002-012
22. The L3 Collaboration, P. Acciari et al., Phys. Lett. B **453**, 83 (1999)
23. G. Altarelli, T. Sjöstrand, F. Zwirner, Physics at LEP2, CERN 96-01 (1996)
24. A. Böhrer, M. Krawczyk, Summary of PHOTON 2001, hep-ph/0203231